

# 52506 Inverse Problems: Part II. Case study: generalized projections

Mikko Kaasalainen  
Tampere University of Technology

November 4, 2011

## Contents

<b>1</b>	<b>Generalized projections of planar curves</b>	<b>3</b>
1.1	Warm-up example: convolution on $S^1$ . . . . .	3
1.2	Classical projections of a planar convex curve . . . . .	3
1.3	Generalized projections . . . . .	5
1.4	Minkowski stability . . . . .	6
1.5	Three-dimensional case . . . . .	7
1.6	Solving for the spin state . . . . .	9
<b>2</b>	<b>Generalized profiles</b>	<b>11</b>
<b>3</b>	<b>Optimal combination of multimodal data: maximum compatibility estimate</b>	<b>12</b>
<b>4</b>	<b>Profile examples</b>	<b>17</b>
<b>5</b>	<b>Project work</b>	<b>20</b>
5.1	General instructions . . . . .	20
5.2	Example: inverse problems of generalized projections in 2-D . . . . .	21
5.2.1	Suggested topics . . . . .	21
5.3	Example: inverse problems of generalized projections in 3-D . . . . .	21
5.3.1	Preliminaries . . . . .	21
5.3.2	Basic linear case . . . . .	22
5.3.3	Statistical inversion: Bayes inference . . . . .	22

5.3.4	Nonlinear form, positivity constraint, regularization . . . . .	23
5.3.5	Setup . . . . .	24
5.3.6	Suggestions and comments . . . . .	24
<b>6</b>	<b>Appendix: Levenberg-Marquardt optimization</b>	<b>25</b>

# 1 Generalized projections of planar curves

## 1.1 Warm-up example: convolution on $S^1$

In convolution on  $S^1$ , the measurements  $m(t)$  of a signal  $f(s)$  blurred with a convolution function  $g(t-s)$ ,  $0 \leq s, t < 2\pi$ , are

$$m(t) = \int_0^{2\pi} g(t-s)f(s) ds, \quad (1)$$

and the functions  $f, g$  can be expressed in Fourier basis:

$$g(x) = \sum_n g_n e^{inx}, \quad f(x) = \sum_n f_n e^{inx}. \quad (2)$$

Thus

$$m(t) = \sum_{kl} g_k f_l e^{ikt} \int_0^{2\pi} e^{i(l-k)s} ds = 2\pi \sum_k g_k f_k e^{ikt}, \quad (3)$$

so if the measured data are given as the Fourier series

$$m(t) = \sum_n y_n e^{int}, \quad (4)$$

we have

$$f_n = \frac{y_n}{2\pi g_n}. \quad (5)$$

If  $g$  is a finite Fourier series, truncated at order  $N$ ,  $m(t)$  contains no data on  $f_n$ ,  $n > N$ . If  $g$  converges rapidly, the reconstruction of the high-order coefficients  $f_n$  greatly amplifies any measurement noise.

Note that convolution is not just a nuisance blurring the signal: mathematically, convolution is necessary to make the signal an observable when the signal is actually a density function (that is never an observable as such). A perfect pinpoint-accurate mask is represented by a Dirac-delta function (otherwise the convolution integral would tend to zero).

If we take the  $S^1$  convolution to be seen on  $\mathbb{R}$ , we have a  $2\pi$ -periodic signal blurred with a  $2\pi$ -wide mask (so we need measurements from an interval at least  $4\pi$  wide). This generalizes directly to convolution on  $T^2 = S^1 \times S^1$ , or on  $\mathbb{R}^2$ . There the convolution mask can be, e.g., cylindrically symmetric, in which case, for  $x, y \in \mathbb{R}^2$ ,

$$g(x, y) = g(\|x - y\|). \quad (6)$$

## 1.2 Classical projections of a planar convex curve

Consider a closed convex curve in  $\mathbb{R}^2$ . It can be uniquely described by a curvature function  $C : S^1 \rightarrow \mathbb{R}$  that describes the length of a segment of the curve at some point described by the direction  $\psi$ ,  $0 \leq \psi < 2\pi$  of the outward normal of the curve

(this is unique since the curve is convex). The tangent direction of the curve at  $\psi$  is thus  $\tau(\psi) = (-\sin \psi, \cos \psi)$ . Now the length  $ds$  of the segment is

$$ds = C(\psi) d\psi, \quad (7)$$

so the curve is uniquely plotted as  $[x(\psi), y(\psi)]$  (up to a translation, so let us start the plot at the origin):

$$x(\psi) = -\int_0^\psi C(\psi') \sin \psi' d\psi', \quad y(\psi) = \int_0^\psi C(\psi') \cos \psi' d\psi'. \quad (8)$$

For the curve to be closed,  $C(\psi)$  must fulfill

$$\oint C(\psi)\tau(\psi) d\psi = \int_0^{2\pi} C(\psi)\tau(\psi) d\psi = 0. \quad (9)$$

If the curvature function  $C$  is given by a real-valued non-negative Fourier series

$$C(\psi) = \Re \sum_n c_n e^{in\psi} \geq 0, \quad n \geq 0, \quad (10)$$

the projected width  $w(\varphi)$  of the curve in the direction  $\varphi$  is

$$w(\varphi) = \int_{-\pi/2}^{\pi/2} C(\psi + \varphi) \cos \psi d\psi. \quad (11)$$

Since the integration limits are symmetric, the only surviving terms from the integrals of  $\cos(n\varphi + n\psi)$  and  $\sin(n\varphi + n\psi)$  are of the form  $\cos n\varphi \cos n\psi$  and  $\sin n\varphi \cos n\psi$ , so we have

$$w(\varphi) = \Re \sum_n c_n e^{in\varphi} I_n, \quad (12)$$

where

$$I_n = \int_{-\pi/2}^{\pi/2} \cos n\psi \cos \psi d\psi \quad (13)$$

and for  $n \neq 1$

$$I_n = \begin{cases} 0 & n = 3, 5, 7, \dots \\ 2/(n^2 - 1) & n = 2, 6, 10, \dots \\ 2/(1 - n^2) & n = 0, 4, 8, \dots \end{cases} \quad (14)$$

and  $c_1 \equiv 0$  since  $I_1 \neq 0$  and we must have  $w(\varphi) = w(\varphi + \pi)$ ; this also fulfills the requirement (9) of a closed curve. Thus  $w(\varphi)$  carries no information on the odd-valued  $n$ -coefficients of the curvature function  $C(\varphi)$  that uniquely defines the shape of the curve. What is more, the effect of the high-order coefficients of  $C$  on  $w$  diminishes rapidly as  $n^{-2}$ , so any errors in  $w$  are greatly blown up in the inverse case of reconstructing  $w \rightarrow C$ .

This situation is exactly the same as in  $\mathbb{R}^3$  for the areas of the projections of convex bodies. A famous example of this is the brightness (lightcurve) of an asteroid at opposition (when the Sun and the Earth are in the same direction as seen from the target). In  $\mathbb{R}^3$ , convex bodies are described as functions on the unit sphere  $S^2$ ; instead of Fourier series, we use spherical harmonics series.

### 1.3 Generalized projections

What can we do to get out of this nonuniqueness and instability problem? To achieve uniqueness, we obviously must have a different type of an experiment. One option is that we do not measure the width of the curve, but its brightness (with some suitable setup: e.g., a tape folded in the shape of the curve). For dark materials, the brightness is directly proportional to the width, but bright materials behave like projection screens. They follow the so-called Lambert scattering law that produces limb darkening. Now our integral  $I_n$  is constructed with a higher power of  $\cos \psi$ :

$$I_n^L = \int_{-\pi/2}^{\pi/2} \cos n\psi \cos^2 \psi d\psi. \quad (15)$$

This is an example of a *generalized projection*. What happens now? We find that this time  $I_n^L = 0$  for even  $n > 2$  and  $I_n^L \neq 0$  for odd  $n$  (exercise), so the situation is reversed: now there is no information on even  $n$  in our measurements.

If we have a combination of both dark and bright materials, we might hope to recover all orders (even though there is still the high-order noise problem). However, we cannot escape a *model noise* problem leading to another instability. Suppose the exponent  $l$  in  $\cos^l \psi$  is  $l \approx 1$  or  $l \approx 2$ : then the odd or even coefficients  $c_n$  are likely to blow up in the same manner as high-order coefficients upon inversion. In other words, the inverse solution is very sensitive to the exact form of the scattering behaviour of the material. This cannot be escaped by any simple trick: we need to redesign our experiment (or observational setup). Note that, in real-world situations, we can *never* expect our model of scattering to be exactly right (and with asteroids  $l$  is very close to 1 at opposition in any case), so our problem should be as robust as possible against the insufficiency of the model.

So let us change the scene: another possibility is to illuminate the target from a different direction than it is viewed. Let the angle between these directions be given by the phase angle  $\alpha$ . Now we only measure the width of the illuminated and visible part of the planar curve (this is another example of a generalized projection), and everything else is either hidden from view or in shadow. Thus we now have

$$w(\varphi) = \int_{-\pi/2+\alpha}^{\pi/2} C(\psi + \varphi) \cos \psi d\psi. \quad (16)$$

Let us write  $C(\psi)$  explicitly as a real-valued Fourier series

$$C(\psi) = \sum_n a_n \cos n\psi + b_n \sin n\psi. \quad (17)$$

Then, if the measurements  $w(\varphi)$  are given as the series

$$w(\varphi) = \sum_n c_n \cos n\varphi + d_n \sin n\varphi, \quad (18)$$

we have

$$c_n = a_n I_n^c(\alpha) + b_n I_n^s(\alpha), \quad d_n = b_n I_n^c(\alpha) - a_n I_n^s(\alpha), \quad (19)$$

where

$$I_n^c(\alpha) = \int_{-\pi/2+\alpha}^{\pi/2} \cos n\psi \cos \psi d\psi, \quad I_n^s(\alpha) = \int_{-\pi/2+\alpha}^{\pi/2} \sin n\psi \cos \psi d\psi, \quad (20)$$

i.e.,  $I_n^s(0) = 0$ . Now the inverse solution  $w \rightarrow C$  is

$$a_n = \frac{I_n^c c_n - I_n^s d_n}{(I_n^c)^2 + (I_n^s)^2}, \quad b_n = \frac{I_n^s c_n + I_n^c d_n}{(I_n^c)^2 + (I_n^s)^2}. \quad (21)$$

(In complex formulation, we could, equivalently, define quantities such as

$$e_n = a_n + ib_n, \quad f_n = c_n + id_n, \quad I_n = I_n^c - iI_n^s, \quad (22)$$

and then have  $f_n = e_n I_n$  so that  $e_n = f_n / I_n$ , where complex division is defined by  $x/y = x\bar{y}/(y\bar{y}) = x\bar{y}/|y|^2$ .)

Obviously, the leading terms of  $w$  are associated with  $I_n^c(\alpha)$  when  $\alpha \approx 0$ . For  $I_n^c(\alpha)$ , we find ( $n > 1$ )

$$I_n^c(\alpha) = \begin{cases} \frac{(-1)^{n/2}}{1-n^2} (1 + \cos n\alpha \cos \alpha + n \sin n\alpha \sin \alpha), & n \text{ even} \\ \frac{(-1)^{(n+1)/2}}{1-n^2} (n \cos n\alpha \sin \alpha - \sin n\alpha \cos \alpha), & n \text{ odd} \end{cases} \quad (23)$$

We see that, for  $\alpha \approx 0$  and  $n$  odd,  $I_n^c(\alpha) = \mathcal{O}(\alpha^3)$ , so the effect of  $\alpha$  is slow at first, but soon considerable as  $\alpha$  grows. In other words, increasing  $\alpha$  brings information on all coefficients of  $C$  to  $w$  and removes nonuniqueness. What is more, it stabilizes the inverse solution:  $I_n^c(\alpha)$  acquires a component proportional to  $n$ , so, for high-order  $n$ ,  $I_n^c(\alpha) \sim 1/n$  rather than the  $1/n^2$  at  $\alpha = 0$ . Thus the observational errors do not blow up as much in direct reconstruction.

#### 1.4 Minkowski stability

We are fortunate to have one more stabilizing factor at play here. This is of great importance in practice, making convex lightcurve inversion of asteroids quite stable. Consider, for example, the integral

$$S_n(\psi) = \int_0^\psi \cos n\psi' \cos \psi' d\psi' \quad (24)$$

defining the contribution of the coefficients  $a_n$  of  $C(\psi)$  in plotting the y-component of the curve  $[x(\psi), y(\psi)]$ . We have ( $n > 1$ )

$$S_n(\psi) = \frac{1}{n^2 - 1} (n \sin n\psi \cos \psi - \cos n\psi \sin \psi). \quad (25)$$

Other integrals contributing to the curve plot are of similar form, all with the factor  $1/(n^2 - 1)$ . Thus this factor cancels out in the inverse chain  $w \rightarrow C \rightarrow (x, y)$ . For example, using the sample integrals calculated above, we see that for small  $\alpha$  the

reconstruction of  $y(\psi)$  yields, for the component dependent on the observed  $c_n$  of (18) ( $n$  even),

$$\sim c_n \frac{n \sin n\psi \cos \psi - \cos n\psi \sin \psi}{1 + \cos n\alpha \cos \alpha + n \sin n\alpha \sin \alpha}. \quad (26)$$

There is a factor of order  $n$  in both numerator and denominator, so we can expect that, as  $\alpha$  grows, the error-amplification factor of the inverse solution is greatly reduced (the full calculation is left as an exercise). This is called *Minkowski stability* as the problem of reconstructing a convex surface (here in  $\mathbb{R}^2$ ) from its curvature function is called the Minkowski problem (Minkowski showed that this is uniquely solvable in  $\mathbb{R}^3$ ).

We thus see that the typical error amplification of order  $n^2$  in  $w \rightarrow C$  is reduced by  $1/n$  by the growing  $\alpha$ , and by a further  $1/n$  in the step  $C \rightarrow (x, y)$  due to Minkowski stability. This explains why it is important to use observations with  $\alpha > 0$ , and why it is more stable to reconstruct a surface than a “painted map” on a sphere (or here a circle). On the other hand, if our observations are based on brightness measurements, and there are first-order terms in the Fourier series of the observed  $w(\psi)$ , we have to conclude that such terms exist in a pseudo- $C$  function in the integrals  $I_1$ . This means that there must be darkness (albedo) variegation on the target. Note carefully that this is only true for our 2-D case: in 3-D, even large first-order terms in the observed Fourier series for brightness are completely normal and easily explainable with shape alone (there the “forbidden terms” are first-degree terms of spherical harmonics instead).

## 1.5 Three-dimensional case

The extension of the 2-D case to  $\mathbb{R}^3$  is considerably more complex, and especially the case of  $\alpha \neq 0$  requires some group theoretical tools for the group  $\text{SO}(3)$  since there are more degrees of freedom than in  $\mathbb{R}^2$ . Nevertheless, the analysis of convex bodies relies on exactly the same principle: we have a chain  $L \rightarrow C \rightarrow x$ , where  $L$  is the volume of the generalized projection on  $S^2 \times S^2$ ,  $C : S^2 \rightarrow \mathbb{R}$  is the curvature function, and  $x \in \mathbb{R}^3$  gives the shape. The basis functions on  $S^2$  are the spherical harmonics  $Y_l^m$ , and with them we can derive the following results [6, 9]:

**Theorem 1.**  $S^2 \times S^2$ -data (i.e.,  $\alpha \neq 0$ ) of the volume of a generalized projection uniquely determine the curvature of a convex compact surface.

Furthermore, Minkowski has shown that the curvature function  $C$  of a convex surface  $\mathcal{B}$  uniquely determines its shape  $x_{\mathcal{B}}$  (up to a translation of  $x$ ), so we can state:

**Corollary.**  $S^2 \times S^2$ -data uniquely determine the shape of a convex compact surface.

**Theorem 2.** The complete mapping  $L \rightarrow x_{\mathcal{B}}$  is continuous for convex bodies in usual topologies (weak \*; the inverse problem is conditionally well-posed in the sense of Tikhonov).

This Minkowski stability is due to the strong stability (continuity) of the Minkowski problem: while the inverse problem  $L \rightarrow C$  is ill-posed, the Minkowski map  $C \rightarrow x_{\mathcal{B}}$  is very stable. In practice, errors in the inferred curvature  $C$  (or surface darkness

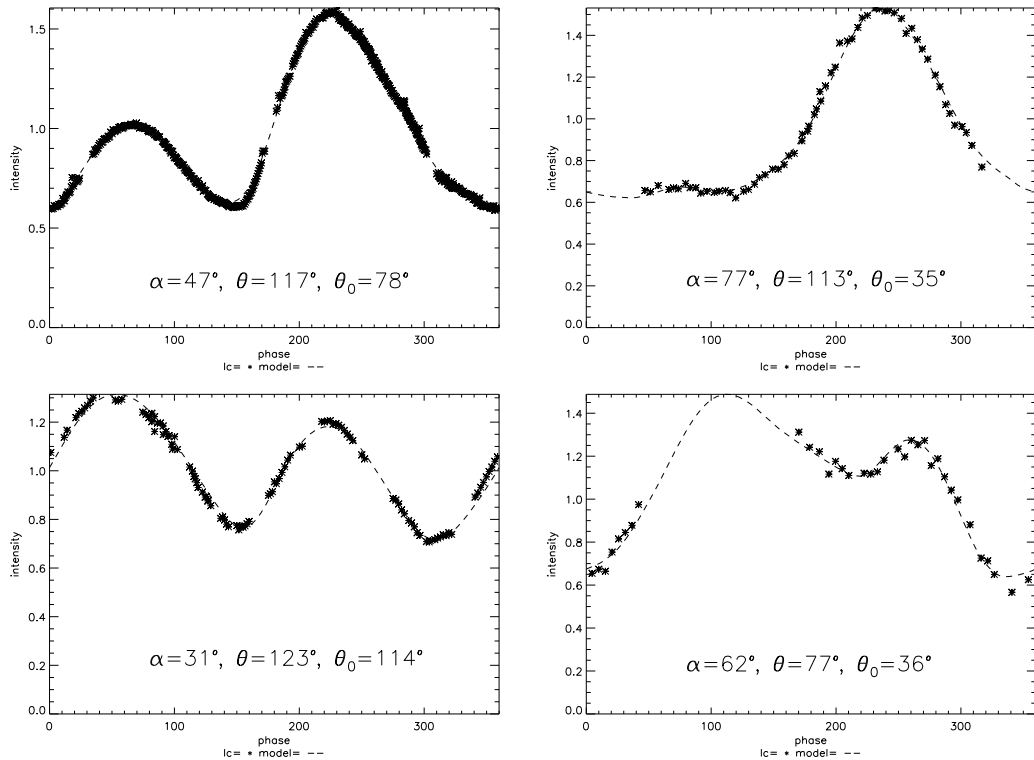


Figure 1: Sample observed (asterisks) vs. modelled (dashed lines) photometric observations (lightcurves) for the asteroid Golevka.

map  $\tilde{C}$ ) on  $S^2$  are larger than the final errors in the shape in  $\mathbb{R}^3$ . Together,  $S^2 \times S^2$ -data and Minkowski stability provide exactly the robustness against the insufficient modellability of the scattering properties that we need. The convexity assumption provides, via Minkowski stability, robustness on the shape solution.

The procedure for obtaining  $L \rightarrow C$  is described and discussed in, e.g., [3, 9, 4, 5]. Some of its basic principles are presented in the project work section here. The numerical procedure for obtaining the map  $C \rightarrow x_B$  is nontrivial (indeed, the uniqueness proofs of Minkowski and Nirenberg are nonconstructive [11, 12]). It can be best represented as an optimization problem in a suitably discretized space (function series coefficients for the radius, or a representation of the shape as a polyhedron), for which a well-converging algorithm can be constructed [3, 9].

Fig. 1 shows sample observations (time series plotted along the azimuthal viewing phase  $\varphi$  of the target) of the asteroid Golevka (with an arbitrarily normalized intensity  $L$ ), together with the modelled  $L$ , and Fig. 2 is a view of the shape reconstruction. The viewing geometries are indicated in the plots (the geometries were obtained with the spin state determination procedure explained below):  $\theta$  is the polar angle of the viewing direction, and  $\theta_0$  that of the illumination direction.

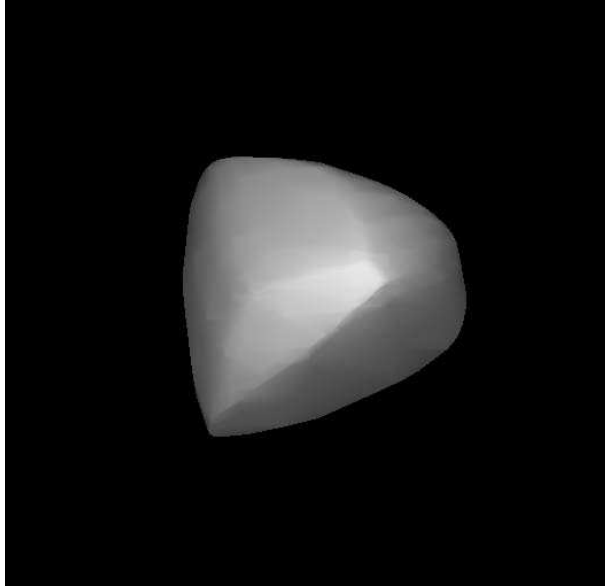


Figure 2: A view of the convex shape reconstruction of Golevka.

## 1.6 Solving for the spin state

Previously we assumed that we know the orientation of the target (and can choose our coordinate system accordingly), but for many targets such as asteroids this is usually not the case. Luckily, the orientation can be determined simultaneously with the shape for asteroids, as we know that an asteroid should be in a physically describable (usually constant) spin state. For most targets, this state is given by the direction of the rotation axis of the body, and the rotation period around this axis, so these three parameters are determined in addition to the shape so that we always know the observation geometries. There is an important ambiguity property for the spin state solution from data obtained in a naturally arising restricted observing geometry. In the following, we prove and discuss this property.

Let  $\mathbf{x} = (x, y, z)$  denote a vector in a coordinate system fixed to the target (i.e., rotating with it,  $z$ -axis aligned with the rotation axis), and  $\mathbf{x}'$  a vector in a nonrotating system (denoted by primes) where the rotation vector points at the direction given by the spherical coordinates  $(\theta', \varphi')$  (rotation is in the positive direction around this vector, with period  $P$ ). Then  $\mathbf{x}'$  and  $\mathbf{x}$  are related by

$$\mathbf{x} = \mathbf{R} \mathbf{x}', \quad (27)$$

where

$$\mathbf{R} = \mathbf{R}_z(\phi_0 + \frac{2\pi}{P}(t - t_0))\mathbf{R}_y(\theta')\mathbf{R}_z(\varphi'), \quad (28)$$

where  $t$  is the time,  $\phi_0$  and the epoch  $t_0$  are some initial values, and  $\mathbf{R}_i(\phi)$  is the rotation matrix corresponding to the rotation of the coordinate frame through angle

$\phi$  counterclockwise about the positive  $i$ -axis. In particular,  $R_z(\phi)$  is

$$R_z(\phi) = \begin{pmatrix} \cos \phi & \sin \phi & 0 \\ -\sin \phi & \cos \phi & 0 \\ 0 & 0 & 1 \end{pmatrix}. \quad (29)$$

**Ambiguity theorem.** If the viewing and illumination directions  $\omega', \omega'_0 \in S^2$  in a nonrotating frame remain in the same plane at all times of observation  $t_i$ , the infinite-distance observations of a body  $\mathcal{B}$ , with surface points  $\mathbf{b} = (x, y, z)$  and rotation vector  $\beta'(\theta', \varphi')$  given in a coordinate system whose equatorial plane is the invariant plane, are indistinguishable from those of a body  $\hat{\mathcal{B}}$  with  $\hat{\mathbf{b}} = (x, y, -z)$  and  $\hat{\beta}' = \beta'(\theta', \varphi' + \pi)$ .

Proof: We choose the invariant plane defined by  $\omega'$  and  $\omega'_0$  as the equatorial plane of the nonrotating system, so the  $z'$ -coordinates of the viewer and the illumination source are zero. From (29) we have

$$R_z(\varphi' + \pi)\mathbf{x}'|_{z'=0} = -R_z(\varphi')\mathbf{x}'|_{z'=0}, \quad (30)$$

so (28) yields

$$\mathbf{x}(\varphi' + \pi, \mathbf{x}'|_{z'=0}) = -\mathbf{x}(\varphi', \mathbf{x}'|_{z'=0}). \quad (31)$$

Since  $\phi_0$  is arbitrary, we can set  $\hat{\phi}_0 = \phi_0 + \pi$  (as  $(x, y) \rightarrow (-x, -y)$  corresponds to a trivial shape rotation of  $\pi$  in the  $xy$ -plane). Therefore a vertical mirror-image shape  $\hat{\mathcal{B}}$  ( $z \rightarrow -z$ ) with a rotation direction changed by  $\varphi' \rightarrow \varphi' + \pi$  has the same viewing and illumination directions with respect to the body shape as  $\mathcal{B}$  and thus yields exactly the same observations as those of  $\mathcal{B}$ .  $\square$

This ambiguity property affects all data that are not two-dimensionally resolved in a plane projection, i.e., in this sense equivalent to observations made at infinity. Thus it appears also with radar data in addition to photometric observations. The coplanarity of  $\omega'$  and  $\omega'_0$  is a case often approximated in the solar system as many targets move close to the plane of the Earth's orbit around the Sun. For such targets, only observations with resolved plane-of-sky projections can properly remove the spin direction ambiguity.

The spin parameters can be added to the problem by using the defining rotation (28) and finding the best-fit parameters with nonlinear optimization (project work section, Appendix, and [4]). The form (28) is based on physical a priori assumption, the so-called relaxed or principal-axis rotation, but other models can be accommodated as well. In fact, it was precisely the inadequacy of (28) for a target (the asteroid 1862 Apollo) that led to the detection of the visible effect of sunlight (photons) on the dynamics of celestial bodies [7]. The inverse problem model had to be expanded by adding an accelerating term (and parameter) to (28) as otherwise the observations could not be explained.

If the time series (lightcurves) of the data set cover many years and apparitions, the period space is filled with densely packed local minima. The smallest separation  $\Delta P$  of the local minima in the trial period  $P$ -spectrum of the  $\chi^2$  of the lightcurve fit is

roughly given by

$$\frac{\Delta P}{P} \approx \frac{1}{2} \frac{P}{T}, \quad (32)$$

where  $T = \max(|t-t_0|)$  within the lightcurve set. This derives from the phenomenon that if  $P$  is changed by  $\Delta P$ , the minima and maxima of the model lightcurve at  $t_0 \pm T$  will undergo a phase shift of  $\pi$  so they will typically be at roughly the same places as with  $P$ . The separation  $\Delta P$  repeats over the whole of the  $\chi^2$ -plot and depends only on the epochs of the lightcurves. The  $P$ -spectrum is also modulated by other, longer  $\Delta P$ 's corresponding to apparition gaps shorter than  $T$ .

## 2 Generalized profiles

Consider the case where images  $\mathcal{I}(\omega, \omega_0)$  obtained at various viewing and illumination directions  $\omega, \omega_0 \in S^2$  are available, but the information in these images is only contained in the boundary curves between the dark background or a shadow and the illuminated portion of the target surface. This situation is typical for faraway objects in space for which low-resolution images are available via large telescopes through adaptive optics (AO) or other deconvolution and image processing techniques. Due to the deconvolution process, the actual brightness levels of the pixels in these images tend to portray artificial and exaggerated features, so they are usually less reliable than profile contours, i.e., the locations of the light/dark boundary pixels [1, 10]. It is possible to show that silhouettes (at  $\omega = \omega_0$ ) uniquely define a large class of bodies (considerably larger than convex ones), and *generalized profiles* (at  $\omega \neq \omega_0$ ) an even larger class [8]. Thus the use of image boundary contours does not actually lose much information even if the image pixels had no systematic errors.

As the coverage of viewing geometries is seldom wide enough to enable a full reconstruction of the model from images alone, we can augment the image dataset with a set of measured brightnesses  $\mathcal{L}(\omega, \omega_0)$  of the target at various observing geometries. The possibility to use images  $\mathcal{I}$  both serves to reconstruct more details in the model than available from  $\mathcal{L}$  (usually they do not reveal nonconvex details [2], i.e., they yield stable solutions only within the convex framework) and to use a combined dataset for successful modelling when neither the available  $\mathcal{L}$  nor  $\mathcal{I}$  are sufficient alone.

Let us now consider the inverse problem of determining the shape and spin state of a body  $\mathcal{B}$  from some measured generalized profiles and the volumes  $L$  of generalized projections. Typically, the profiles are obtained at restricted geometries and their resolution level is not high. When a dense coverage of geometries and high resolution are available, direct methods of computer vision and cartography are usually applicable.

Our goal is to construct a total goodness-of-fit measure  $\delta_{\text{tot}}$

$$\delta_{\text{tot}} = \delta_L + \lambda_{\partial} \delta_{\partial} + \lambda_R g(P), \quad (33)$$

where  $L$  denotes lightcurves,  $\partial$  generalized profiles, and  $R$  regularizing functions  $g(P)$ , where  $P \in \mathbb{R}^p$  is the vector of model parameters. The modelling of  $\delta_{\partial}$  is

discussed in [8]. The parameters  $P$  describing the target usually have to be (moderately) regularized to prevent unrealistic solutions. One aspect is the smoothness of the body; the larger the target is, the less irregular it is expected to be. For some parts of the surface this is explicitly enforced by the profile data, so the regularization mostly pertains to the parts covered only by lightcurves that contain little information on nonconvex features. In those regions, undulation of the surface should be suppressed (the optimal choice of the suppression weight is discussed below).

For example, for starlike bodies  $\mathcal{B}$ , a simple (computationally  $\chi^2$ -like) measure of global regularity is

$$g_S = \int_{\mathcal{B}} [r - \langle r \rangle]^2 d\sigma, \quad (34)$$

where  $r$  is the radius of the model at the point corresponding to the surface element  $d\sigma$ ; for polytopes, we can simply use  $g_S = \sum_i (r_i - \langle r \rangle)^2$ . For such bodies,  $g_S$  is typically quite efficient when the radius is given by a truncated Laplace series (itself a smoothing agent) and the regularization weight is low. Other typical regularization functions based on local smoothness or physical constraints are discussed in [8].

Now we have an important problem to solve: how to choose the weights  $\lambda$ ? How do we define a best solution when we have two (or more) completely different data modalities?

### 3 Optimal combination of multimodal data: maximum compatibility estimate

Let us choose as goodness-of-fit measures (from which probability distributions can be constructed as well) some  $\delta_i$ -functions,  $i = 1, \dots, n$ , of  $n$  data modalities. Our task is to construct a joint  $\delta_{\text{tot}}$  with well-defined weighting for each data mode:

$$\delta_{\text{tot}}(P, D) = \delta_1(P, D_1) + \sum_{i=2}^n \lambda_{i-1} \delta_i(P, D_i) \quad D = \{D_i, i = 1, \dots, n\} \quad (35)$$

(to which regularization functions  $g(P)$  can be added), where  $D_i \in \mathbb{R}^{m_i}$  denotes the data from the source  $i$ , and  $P \in \mathbb{R}^p$  is the set of model parameter values. The functional form for  $\delta \in \mathbb{R}$  is any pointwise directly additive goodness-of-fit measure so that  $\delta_{\text{tot}}$  retains the same form as each  $\delta_i$ . Also,  $\delta \geq 0$  and  $\delta(P, D)$  is continuous in  $P$  and  $D$ . For the  $L_k$ -norm,

$$\delta_i(P, D_i) = \|\mathcal{M}_i(P) - D_i\|_k^k$$

( $k = 1$  for total variation or  $k = 2$  for least squares), where  $\mathcal{M}_i(P) \in \mathbb{R}^{m_i}$  is the vector of the model function values corresponding to the measured  $D_i$ . Alternatively,  $\delta$  can be the  $\chi^2$ -type variation of  $L_2$  that uses the estimated noise level for each point as a weighting factor. In lightcurve measurements, for example, the effect of systematic errors in both model and data dominates over random noise when the

noise level is not high, so it is not mandatory to use  $L_2$  or  $\chi^2$  as a standard measure of fit. When probability densities such as a posteriori distributions are constructed from  $\delta_{\text{tot}}$ , one can assume  $\delta$ -based distributions only for the data components, and other suitable (prior) distributions for the regularization components such that the maximum of the a posteriori distribution occurs at  $\arg \min \delta_{\text{tot}}(P)$ .

Instead of expressing full weight for the mode  $D_i$ ,  $i > 1$ , by  $\lambda_{i-1} \rightarrow \infty$ , we can equivalently write  $\delta_{\text{tot}}$  with finite weights  $\hat{\lambda}_i$  as

$$\delta_{\text{tot}}(P, D) = (1 - \sum_{i=1}^n \hat{\lambda}_i) \delta_1(P, D_1) + \sum_{i=2}^n \hat{\lambda}_{i-1} \delta_i(P, D_i),$$

where the transformations  $\lambda \leftrightarrow \hat{\lambda}$ , with  $\lambda, \hat{\lambda} \in \mathbb{R}^{n-1}$ , are

$$\begin{aligned} \hat{\lambda}_i &= \frac{\lambda_i}{1 + \sum_j \lambda_j}, & 0 \leq \sum_i \hat{\lambda}_i \leq 1 \\ \lambda_i &= \frac{\hat{\lambda}_i}{1 - \sum_j \hat{\lambda}_j}, & \lambda_i \geq 0. \end{aligned}$$

We will use the  $\lambda$ -notation here due to its simplicity, with the understanding that  $\lambda_i = \infty$  means a specific case rather than a limit: all modes with  $\lambda_i = \infty$  have equal weights, other modes zero weights.

For a given weight vector  $\lambda \in \mathbb{R}^{n-1}$  we denote

$$P_\lambda(D, \lambda) := \arg \min_P \delta_{\text{tot}}(P, D)|_\lambda, \quad (36)$$

and we want to define an optimal  $\lambda = \lambda_0$  yielding the corresponding estimate  $P_\lambda(D, \lambda_0)$ . For the purposes of this section,  $D$  is fixed so we drop it from the notations below. We assume the  $\delta_i$ -space to be nondegenerate, i.e.,

$$\arg \min \delta_i(P) \neq \arg \min \delta_j(P), \quad i \neq j \quad (37)$$

(in the degenerate case we would have no  $\lambda$ -problem to solve, i.e., the values of  $\lambda_i$  do not affect  $\arg \min \delta_{\text{tot}}$ ). Note that this nondegeneracy is not only due to random errors in  $D_i$  but stems from the typical issues in inverse problems:

1. The models for different modalities are insufficient. This can be termed approximation or modelling error.
2. There are systematic errors in the data.
3. The model is nonunique or unstable either intrinsically or due to sparse coverage of the data space. For example, some or all of the data modes may be insufficient alone for a unique model.

Let us define the mapping  $\chi : \mathbb{R}^p \rightarrow \mathbb{R}^n$

$$\chi_i(P) = \log[\delta_i(P)], \quad i = 1, \dots, n$$

from the parameter space  $\mathbb{R}^p$  into  $\log \delta_i$ -space, and the region  $\mathcal{R} \subset \mathbb{R}^n$ :

$$\mathcal{R} = \{\chi(P) | P \in \mathcal{P}\}$$

where the set  $\mathcal{P}$  includes all the possible realizations of the model parameter vector  $P$  ( $\chi$  is continuous so  $\mathcal{R}$  is connected at least for a connected  $\mathcal{P}$ ). Further, let us write the mapping  $\mathcal{S} : \mathbb{R}^{n-1} \rightarrow \mathbb{R}^n$ :

$$\mathcal{S}(\lambda) = \chi[P_\lambda(\lambda)], \quad \lambda \in \mathbb{R}^{n-1},$$

where  $P_\lambda(\lambda)$  is given by (36).

For simplicity (and in accordance with our case study), we next consider the case of two data modalities:  $n = 2, \lambda \in \mathbb{R}$ . The end points of the curve  $\mathcal{S}(\lambda)$  are now at  $\lambda = 0$  and  $\lambda = \infty$ , i.e., at the values of  $\delta_i$  that result from using only one of the data modes in inversion. This can be directly generalized to  $n > 2$ , as we will show below.

**Proposition.** Under the mapping  $\chi$ , the image  $\mathcal{S}(\lambda)$  of the parameter vector  $P_\lambda \in \mathbb{R}^p$  corresponding to a given weight vector  $\lambda$ :

$$P_\lambda(\lambda) = \arg \min_P \delta_{\text{tot}}(P)|_\lambda,$$

lies on  $\partial\mathcal{R}$ :  $\mathcal{S}(\lambda) = \chi(P_\lambda) \in \partial\mathcal{R}$ .

*Proof.* Since  $P_\lambda$  minimizes

$$\delta_{\text{tot}} = \delta_1(P) + \lambda\delta_2(P),$$

there can be no images  $\chi(P) \in \mathcal{R}$  with  $\delta_1(P) < \delta_1(P_\lambda)$  and  $\delta_2(P) < \delta_2(P_\lambda)$  as otherwise we would have  $\delta_{\text{tot}}(P) < \delta_{\text{tot}}(P_\lambda)$ . Since  $\chi(P_\lambda) \in \mathcal{R}$ , and there are no points in  $\mathcal{R} \in \mathbb{R}^2$  both below and to the left of  $\chi(P_\lambda)$ , necessarily  $\chi(P_\lambda) \in \partial\mathcal{R}$ .  $\square$

**Remark.** Even though the images  $\chi(P_\lambda)$  reside on part of the boundary  $\partial\mathcal{R}$  connecting the points  $\chi[P_\lambda(0)]$  and  $\chi[P_\lambda(\infty)]$ , the values  $0 \leq \lambda < \infty$  do not necessarily cover the whole of this part, i.e., the image curve  $\mathcal{S}(\lambda) = \chi[P_\lambda(\lambda)]$  is not necessarily connected.

**Definition.** A  $\lambda$ -discontinuity occurs when  $P_\lambda(\lambda)$  is discontinuous. Then the image  $\mathcal{S}(\lambda) = \chi[P_\lambda(\lambda)]$  is discontinuous along  $\partial\mathcal{R}$  (and at each discontinuity value  $\lambda_d$  there is more than one point  $\mathcal{S}(\lambda_d)$ ).

For example, the  $L$ -data typically may have two almost as plausible solution regions in  $\mathbb{R}^p$ , while the profile data only point to one of these (this is due to the nonuniqueness condition discussed earlier). Depending on the data, the solution based on  $L$ -data only may prefer the wrong region and subsequently jump to the correct region in  $\mathbb{R}^p$  as  $\lambda$  is increased. This causes a  $\lambda$ -discontinuity.

We can now denote

$$\begin{aligned} x(\lambda) &= \chi_1[P_\lambda(\lambda)] = \log \delta_1[P_\lambda(\lambda)], \\ y(\lambda) &= \chi_2[P_\lambda(\lambda)] = \log \delta_2[P_\lambda(\lambda)], \end{aligned} \tag{38}$$

so the mapping  $\mathcal{S} : \mathbb{R} \rightarrow \mathbb{R}^2$  is

$$\mathcal{S}(\lambda) := [x(\lambda), y(\lambda)]. \quad (39)$$

The curve  $\mathcal{S}(\lambda)$  resembles the well-known ‘‘L-curve’’ related to, e.g., Tikhonov regularization. However, here we make no assumptions on the shape of  $\mathcal{S}$ . The parameter  $\lambda$  describes the position on  $\mathcal{S}$ , and it is up to us to define a criterion for choosing the optimal value of  $\lambda$ . The logarithm ensures that the shape of  $\mathcal{S}(\lambda)$  is invariant under unit or scale transforms in the  $\delta_i$  as they merely translate  $\mathcal{S}$  in the  $(\log \delta_1, \log \delta_2)$ -plane. It also provides a meaningful metric for the  $\log \delta_i$ -space: distances depict the relative difference in  $\delta$ -sense, removing the problem of comparing the absolute values of quite different types of  $\delta_i$ .

The shape of the  $\mathcal{S}$ -curve is a diagnostic marker of the cases 1-3 mentioned in connection with (37). If  $\mathcal{S}$  resembles a line parallel to the coordinate axis of one data mode, the solution corresponding to the other mode is nonunique or unstable. The more  $\mathcal{S}$  resembles ‘‘L’’ (a sharp corner), the more the nondegeneracy of the  $\delta_i$ -space is due to the case 3 for both modes, whereas a more blunt (or even diagonal) curve increasingly indicates cases 1 or 2. For example, in Fig. 3a cases 1 and 2 have a clear contribution, while in Fig. 3b case 3 dominates. In this case this is mostly due to the nonuniqueness of the shape solution from lightcurves in nonconvex space. Silhouette data single out the real nonconvex features from the many possibilities afforded by lightcurves (the convex solution, in a way an average ‘‘convex hull’’ of these possibilities, is unique for them).

Similarly, the span of  $\mathcal{S}$  along the  $\delta_i$  axes serves as a diagnostic tool. If the nondegeneracy (37) were only due to random errors in data,  $\mathcal{S}$  would be a short curve, i.e., augmenting one dataset by another mode does not add very much information. The longer the span of  $\mathcal{S}$  along one  $\delta_i$ -axis, the more there is instability (or nonuniqueness) corresponding to the data mode  $i$ , and the more the other data modes add information.

We can translate the origin of the  $(\log \delta_1, \log \delta_2)$ -plane to a more natural position by choosing the new coordinate axes to pass through the end points of  $\mathcal{S}$ . Denote

$$\begin{aligned} X &= x(\lambda)|_{\lambda=0} = \log \min \delta_1 \\ Y &= y(\lambda)|_{\lambda \rightarrow \infty} = \log \min \delta_2. \end{aligned} \quad (40)$$

Then  $(X, Y)$  is the new origin in the  $(x, y)$ -plane. A natural choice for an optimal location on  $\mathcal{S}$  is the point closest to  $(X, Y)$ .

**Definition.** The parameter vector  $P_0 \in \mathbb{R}^p$  such that

$$P_0 = \arg \min_P \left( [\log \delta_1(P) - X]^2 + [\log \delta_2(P) - Y]^2 \right) \quad (41)$$

is called the *maximum compatibility estimate* (MCE). The *maximum compatibility weight* (MCW)  $\lambda_0$  is given by

$$\lambda_0 = \arg \min_{\lambda} \left( [x(\lambda) - X]^2 + [y(\lambda) - Y]^2 \right). \quad (42)$$

In this approach, neither the numbers of data points in each  $\delta_i$  nor the noise levels of data modes explicitly affect the solution for the optimal  $P_0$  as their scaling effects cancel out in each quadratic term (when  $\delta_i$  are based on  $L_k$ ).  $P_0$  is thus a pure compatibility estimate describing the best model compromise explaining the datasets of different modes simultaneously. Instead of the  $L_2$ -norm for the distance from  $(X, Y)$ , we could use other definitions just as in  $\delta$ , but this seldom essentially changes the result.

The maximum compatibility estimate corresponds to the maximum likelihood estimate in the case of one data mode, or to the maximum a posteriori estimate as well since we can include regularization functions here. If regularizing is used, the weights for the functions are either determined in a similar manner (see below), or they can be fixed and the regularization terms are absorbed in  $\delta_1$  (otherwise  $\mathcal{S} \subset \partial\mathcal{R}$  does not hold). MCE is not necessarily unique.

**Definition.** A multimodal inverse problem is *self-consistent* if there exists a  $\lambda_0$  corresponding to  $P_0$ , i.e., the image  $\chi(P_0)$  of the MCE is on  $\mathcal{S}$ :

$$\exists \lambda_0 : P_0 = P_\lambda(\lambda_0).$$

If a problem is not self-consistent, one should be cautious of accepting either the MCE  $P_0$  (41) or the MCW-based estimate  $P_\lambda(\lambda_0)$  as the solution. If the two are significantly different, this may be an indication of systematic errors in data or in the models causing fundamental incompatibility.

The self-consistency principle and the above analysis of systematic errors can be extended to all inverse problems (also single-mode ones) by considering subsets of the complete dataset. For example, one can estimate the optimal weight for one lightcurve that appears to reveal features not contained in other lightcurves and thus judge its real significance. Even one noisy lightcurve with a few points, taken at a special observing geometry, may well contain significant information that needs to be weighed more against less noisy but more ordinary lightcurves. Note that  $\lambda$ -discontinuity can also occur for only one data mode if we partition the dataset into subsets.

A choice frequently used in the L-curve approach is to find the  $\lambda$  at which  $\mathcal{S}$  attains its maximum curvature, but evaluating this point is less robust than finding  $\lambda_0$ , and (42) is a more natural prescription, requiring no assumptions on the shape of  $\mathcal{S}$ . Besides,  $\lambda$ -discontinuities can be induced by regularization as well, i.e., the “L-curve” is not necessarily even connected.

Note that we can locate the point estimate MCE  $P_0$  with standard optimization procedures and with essentially no extra computational cost added to that of solving for any  $P_\lambda$ . However, it is useful (though computationally somewhat noisier) to approximate  $\mathcal{S}$  via the minimization of  $\delta_{\text{tot}}$  with sample values of  $\lambda$  (see Fig. 1), as in addition to obtaining the MCW  $\lambda_0$  (and hence MCE as well for self-consistent cases) we can plot  $\mathcal{S}$  to examine the mutual behaviour of the complementary data sources. What is more, the quantity  $[\log \delta_1(P) - X]^2 + [\log \delta_2(P) - Y]^2$  may have more than one local minimum in  $\log \delta_i$ -space, so another reason for plotting  $\mathcal{S}$  is

to ensure that we have found the global minimum (or minima). Furthermore, the solution for  $\lambda_0$  is needed for constructing distributions based on  $\delta_{\text{tot}}$ .

The MCE should also be feasible: if we have upper limits  $\epsilon_i$  to acceptable  $\delta_i$ , the feasible region  $\mathcal{F}$  is the rectangle  $\bigcap_i \{\log \delta_i \leq \log \epsilon_i\}$ . If  $[\log \delta_1(P_0), \log \delta_2(P_0)] \notin \mathcal{F}$  and  $\mathcal{F} \cap \mathcal{R} \neq \emptyset$ , we choose the feasible point on  $\mathcal{S}$  closest to the point corresponding to  $\lambda_0$  (i.e.,  $\log \delta_i = \log \epsilon_i$  for one  $i$ ). If  $\mathcal{F} \cap \mathcal{R} = \emptyset$ , the data modes do not allow a compatible joint model, so either the model is incorrect for one or both data modes, or one or both  $\epsilon_i$  have been estimated too low (e.g., systematic errors have not been taken into account). Model insufficiency should also be taken into account in the estimation of  $\epsilon_i$ .

This approach and the results above are straightforwardly generalized to  $n$   $\delta$ -functions and  $n - 1$  parameters  $\lambda_i$  describing the position on the  $n - 1$ -dimensional boundary surface  $\partial\mathcal{R}$  of an  $n$ -dimensional domain  $\mathcal{R}$  and on a hypersurface  $\mathcal{S} \subset \partial\mathcal{R}$ . The MCE is

$$P_0 = \arg \min \sum_{i=1}^n \left[ \log \frac{\delta_i(P)}{\delta_{i0}} \right]^2, \quad \delta_{i0} := \min \delta_i(P), \quad (43)$$

and the MCW is, with  $\lambda \in \mathbb{R}^{n-1}$ ,

$$\lambda_0 = \arg \min \sum_{i=1}^n \left[ \log \frac{\hat{\delta}_{i,\text{tot}}(\lambda)}{\delta_{i0}} \right]^2, \quad \hat{\delta}_{i,\text{tot}}(\lambda) := \left\{ \delta_i \mid \min \delta_{\text{tot}}; \lambda \right\}. \quad (44)$$

Another scale-invariant version of MCE can be constructed by plotting  $\delta_i$  in units of  $\delta_i/\delta_{i0}$  and shifting the new origin to  $\delta_i/\delta_{i0} = 1$ :

$$P_0 = \arg \min \sum_{i=1}^n \left[ \frac{\delta_i(P)}{\delta_{i0}} - 1 \right]^2, \quad \lambda_0 = \arg \min \sum_{i=1}^n \left[ \frac{\hat{\delta}_{i,\text{tot}}(\lambda)}{\delta_{i0}} - 1 \right]^2. \quad (45)$$

This, however, is exactly the first-order approximation of (43) and (44) in  $\sigma \ll 1$  when  $\delta_i/\delta_{i0} = 1 + \sigma$ , giving virtually the same result as (43) and (44) as usually  $\delta_i(P_0)/\delta_{i0} - 1 \ll 1$  in the region around  $\delta_i(P_0)$ , and any larger ratios of  $\delta_i/\delta_{i0}$  are not eligible for the optimal solution (see Fig. 3).

It is possible to use this approach for general regularizing functions  $g(P)$  as well (change  $\delta_i \rightarrow g(P)$  for some  $i$ ), but in such cases the shape of  $\mathcal{S}$  must be taken into account. If it is possible to have a solution  $g(P') = 0$  for a regularizing function  $g$  (or an almost vanishing  $g(P')$  such that  $\log g(P') \rightarrow -\infty$ ), the above scheme automatically returns  $P'$  and ignores the actual data altogether. Thus one should, e.g., set a lower practical limit to  $g(P)$  by looking at the shape of  $\mathcal{S}$ , and choose the  $\lambda_0$  within the restricted part of  $\mathcal{S}$ .

## 4 Profile examples

As examples of the optimal combining of lightcurves and AO profiles, we show representative results for the asteroids 2 Pallas and 41 Daphne. The observed profiles

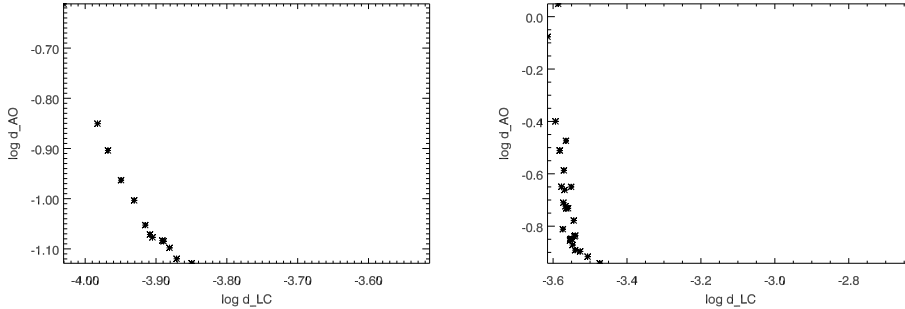


Figure 3:  $\mathcal{S}$  curve plotted for two asteroids with various weights  $\lambda$  (LC for lightcurves, AO for adaptive optics profiles). Left: 2 Pallas, right: 41 Daphne

are projections of the target on the plane-of-sky  $S^2$  converted to pixels on the instrument plane, while the model is constructed in absolute (km) size, so the model/profile scale conversion is given by the AO instrument's angular resolution and the distance between the target and the observer.

In general, the resolution of the model must be somewhat lower than the apparent resolution of the AO images as the sparse profile samples will produce artificial features elsewhere in the model if a near-perfect profile fit is enforced (even if the observed profile details were exactly right). The inverse problem has thus some ill-posedness at local scales starting near the profile resolution level, but the ill-posedness at more global scales, inherent to lightcurve data, is removed with AO profiles. The weight factor  $\lambda$  mostly takes care of this, and fine-tuning is obtained with  $\lambda_S$  for the smoothness constraint  $g_S$ .

Fig. 3 depicts typical evaluations of the curve  $\mathcal{S}$  at various choices of  $\lambda$ ; or rather, this plot portrays the cross-section of the 2-surface  $\partial\mathcal{R}$  in  $\mathbb{R}^3$  with  $\lambda_S$  fixed at its final optimal value. The values for  $\delta_i$  are normalized to be the rms deviations of model fits  $d_i = \sqrt{\delta_i/N_i}$ , as in logarithmic scale this corresponds only to a shift of origin and a uniform linear change of plot scaling. The plotted points outline the curve  $\mathcal{S}(\lambda)$  that is rather an oblique line than an L-shape, and the ideal point region, i.e., the point closest to the lower left-hand corner, can directly be found. As can be seen from Fig. 3, computational noise in the estimated points at  $\lambda = 0$  and  $\lambda = \infty$ , corresponding to a small change of the position of the new origin w.r.t.  $\mathcal{S}$ , does not affect the estimated location of the optimal point on  $\mathcal{S}$  significantly.

Sample observed vs. modelled profiles for 2 Pallas and 41 Daphne are shown in Figs. 4 and 5. The starlike surface model was described by the exponential Laplace (spherical harmonics) series for the surface radius  $r$

$$r(\theta, \varphi) = \exp \left[ \sum_{lm} c_{lm} Y_l^m(\theta, \varphi) \right], \quad (\theta, \varphi) \in S^2, \quad (46)$$

truncated at suitable  $l, m$ , with  $c_{lm}$  as the shape parameters to be solved for. Other model parameters are the profile offset  $(\xi_0, \eta_0)$  for each image and the spin param-

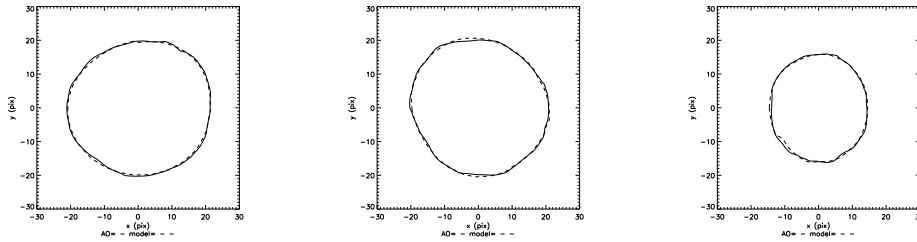


Figure 4: Sample observed (solid lines) vs. modelled (dashed lines) AO contours for 2 Pallas. Coordinates are in pixel units.

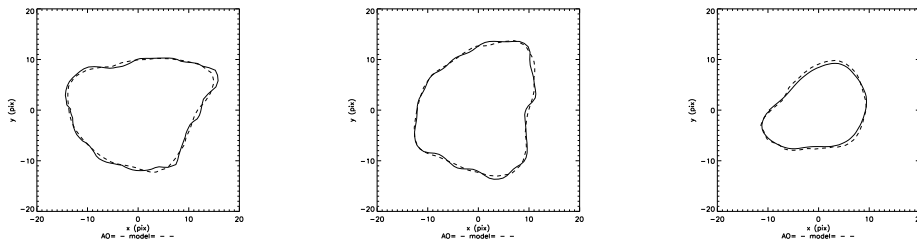


Figure 5: Sample observed (solid lines) vs. modelled (dashed lines) AO contours for 41 Daphne. Coordinates are in pixel units.

eters. For asteroid 2 Pallas (a rather spherical body with size class 500 km), the Laplace series was truncated at maximal  $l = 6, m = 6$ , while for the more irregular 41 Daphne (size class 200 km) the truncation point  $l = 8, m = 6$  was more appropriate. The early truncated Laplace series and the choice of the truncation point are implicit regularization measures as such.

Once the weight factors  $\lambda$  and  $\lambda_S$  are determined, the result is usually stable and restricted to one region in the parameter space  $\mathbb{P}$ : probing feasible solutions  $P$  corresponding to  $\delta_{\text{tot}}(P)$  slightly lower than  $\delta_{\text{tot}}(P_0)$  produces essentially the same results. Due to restricted orbital geometries, lightcurve data alone often imply two almost equally possible pole directions with mirror-like shape; even one AO (or other) image usually resolves this typical ambiguity (as discussed above, this may lead to a  $\lambda$ -discontinuity, though usually not in the vicinity of the MCE). The result is also typically stable with respect to weight values  $\lambda$  around the MCW  $\lambda_0$ . The obtained MCE appears to be well justified when one samples the solutions along  $\mathcal{S}$ : it provides a very good match to profile details without straying far from the observed lightcurves, and does not predict too prominent features on the parts of the surface not projected onto the profile contours.

## 5 Project work

### 5.1 General instructions

The goal of the project work is to examine different approaches and aspects of the reconstruction of a signal from noisy observations of a convolution-type system. The idea is to create the setup and inversion programs from scratch for a proper understanding of the problem.

Choose one of the following cases:

1. Convolution in  $\mathbb{R}^2$ : design original signals and convolution masks, create data with various noise levels, and then try reconstruction schemes (for formulation see lecture notes, Part I)
2. Tomography in  $\mathbb{R}^2$ : design a density distribution in some domain, create various tomographic line integrals and add noise, then reconstruct the distribution (for formulation see lecture notes, Part I)
3. Generalized projections on  $S^1 \times S^1$  (see below): examine the stability properties of the reconstruction of a planar curve analytically and numerically
4. Generalized projections on  $S^2 \times S^2$  (see below): create noisy data of the total brightness of a “world map” seen at different geometries, and reconstruct the map.

The project work report ( $\geq 7$  pages) should be organized in the form of a scientific paper, including at least the following sections:

- A short introduction and background
- Your problem and simulation setup
- Methods and results
- Analysis of results, conclusions, discussion
- References

Use any software packages and programming languages you like. Use your imagination: just about all “typical” theoretical and practical aspects of inverse problem solving are encountered in these problems. Approach this as something studied for the first time: what would we like to know? What approaches should we try? Plot

- your solutions vs. original signal
- model fits vs. data.

You can get up to 15 extra points with this work. The project can be done in groups of  $\leq 3$  people. For examples, read the descriptions below. The same general approach applies to all of the cases above.

## 5.2 Example: inverse problems of generalized projections in 2-D

Here we study the case of a planar convex curve: how to obtain its shape from the volumes of its generalized projections (see lecture notes above).

### 5.2.1 Suggested topics

1. Calculate explicitly all the integrals determining the relationship between the Fourier series of the curvature function  $C(\psi)$  and that of the observations  $w(\varphi)$ , when  $\alpha \neq 0$ . Examine stability properties with growing  $\alpha$  and order  $n$ ; check numerically. Calculate the integrals determining the curve from its  $C(\psi)$  and examine stability as above. Create some convex shape with a positive Fourier series, add some noise to the Fourier coefficients of its observed  $w$ , invert back, and plot the result. How much do the curves differ?
2. As above, but for the Lambert law: now the factor in the integrand is  $\cos \psi \cos(\psi - \alpha)$  instead of  $\cos \psi$ .
3. Examine the stability properties with respect to the assumed scattering law when  $\alpha$  grows: supposing the integrand factor to be of the form  $\cos \psi [1 - k + k \cos(\psi - \alpha)]$ , how are the determined coefficients and the shape plot affected when observations created with  $k$  are inverted with some incorrect  $k' \neq k$ ? Investigate numerically (e.g.,  $k = 0.2$  and  $k' = 0.3$ ).
4. Rather than use Fourier series, create observed values at a set of  $\varphi$ , add some random noise to these, and determine the Fourier coefficients of  $C$  by solving the corresponding set of linear equations. What is the condition number of the system matrix? Use SVD or Bayes as described below. Plot the resulting planar curve.

## 5.3 Example: inverse problems of generalized projections in 3-D

### 5.3.1 Preliminaries

We consider a convex polyhedron  $\mathcal{B}$  with given vertices and their circuits for facets, i.e., we know the areas and normals of the facets. The shape can be anything convex, e.g., an approximated sphere (see below). Our unknowns are the darkness values of the facets:  $0 < g_i \leq 1$ ,  $i = 1, \dots, M$ . From  $g \in \mathbb{R}^M$ , the observations  $L \in \mathbb{R}^N$  are, in  $(\omega_0, \omega) \in S^2 \times S^2$  giving the illumination and viewing directions

$$L(\omega_0, \omega) = A(\mathcal{B}; \omega_0, \omega)g, \quad (47)$$

where the matrix  $A$  is given by the shape of  $\mathcal{B}$  and the geometry:

$$A_{ij} = S_j \left( \mu^{(ij)}, \mu_0^{(ij)} \right) \sigma_j, \quad (48)$$

where  $S_j$  and  $\sigma_j$  are the scattering model and surface area of facet  $j$ ;  $\mu^{(ij)} = \omega_i \cdot \nu_j$  and  $\mu_0^{(ij)} = \omega_{0i} \cdot \nu_j$ , where  $\omega_i$  and  $\omega_{0i}$  are the viewing and illumination directions for

the observation  $i$ , and  $\nu_j \in S^2$  is the unit outward normal of facet  $j$ . For  $\mu^{(ij)} \leq 0$  or  $\mu_0^{(ij)} \leq 0$ ,  $A_{ij} = 0$  due to convexity.

### 5.3.2 Basic linear case

Find the minimum of

$$\|L - Ag\|_2^2 = \sum_{i=1}^N \left( L_i - \sum_{j=1}^M A_{ij} g_j \right)^2. \quad (49)$$

The most basic linear solution is obtained from

$$(A^T A)g = A^T L. \quad (50)$$

Add random noise:  $L \rightarrow L + \epsilon$  and try again. Can you stabilize with SVD: write

$$A = U W V^T, \quad (51)$$

and then, in

$$A^{-1} = V[\text{diag}(1/w_j)]U^T \quad (52)$$

set suitable diagonal elements to zero. With a stabilized matrix

$$\tilde{A} = \text{diag}(w_j)_{j \leq M'}, \quad M' \leq M, \quad (53)$$

we have

$$g = \sum_{j=1}^{M'} \left( \frac{U_{(j)} \cdot L}{w_j} \right) V_{(j)} \quad (54)$$

(where  $U_{(j)}, V_{(j)}$  are the columns  $j$  of the matrices  $U, V$  as vectors).

### 5.3.3 Statistical inversion: Bayes inference

If we assume Gaussian distributions, our linear model yields a simple maximum likelihood estimate  $\hat{g}$  for the posterior distribution. Let our a priori distribution be concentrated around  $g_0$  (with tightness and correlation given by the matrix  $\Sigma_0$ ):

$$p_{pr}(g) \sim \exp\left[-\frac{1}{2}(g - g_0)^T \Sigma_0^{-1}(g - g_0)\right]. \quad (55)$$

On the other hand, the conditional distribution of the measurement is

$$p(L|g) \sim \exp\left[-\frac{1}{2}(L - Ag)^T \Sigma_1^{-1}(L - Ag)\right], \quad (56)$$

where  $\Sigma_1$  is the covariance matrix of the measurements ( $\Sigma_{ij} = \langle \epsilon_i \epsilon_j \rangle$ ). Then Bayes says

$$p(g|L) \sim p_{pr}(g)p(L|g) \quad (57)$$

so we obtain

$$p(g|L) \sim \exp\left\{-\frac{1}{2}[g^T Q g - 2g^T Q Q^{-1}(\Sigma_0^{-1} g_0 + A^T \Sigma_1^{-1} L) + \dots]\right\} \quad (58)$$

where the Fisher information matrix is

$$Q = (\Sigma_0^{-1} + A^T \Sigma_1^{-1} A). \quad (59)$$

Thus our posterior distribution is the exponential quadratic form

$$p(g|L) \sim \exp\left[-\frac{1}{2}(g - \hat{g})^T Q (g - \hat{g})\right] \quad (60)$$

with the centre of the posterior distribution  $\hat{g}$  at

$$\hat{g} = Q^{-1}(\Sigma_0^{-1} g_0 + A^T \Sigma_1^{-1} L). \quad (61)$$

The formal error estimates (squared) for the parameters  $\hat{g}_j$  are the diagonal elements of  $Q^{-1}$ . If the a priori part is uniform, we simply get the old LSQ normal equations.

### 5.3.4 Nonlinear form, positivity constraint, regularization

Instead of  $g$ , we can solve for  $a \in \mathbb{R}^M$  as the parameters in

$$g_j = e^{a_j} \quad (62)$$

to ensure positivity. Levenberg-Marquardt optimization (see appendix) is useful for this, as now our objective function (49) is of the nonlinear least-squares form

$$\chi^2 = \sum_{i=1}^N [f(a; (\omega_0, \omega)_i) - L_i]^2. \quad (63)$$

Simple regularization functions  $R(g)$  for

$$g = \arg \min\{\chi^2 + \lambda R(g)\} \quad (64)$$

can be added in pseudo- $\chi^2$  form (so we can use L-M), e.g.,

$$R(g) = \sum_{i=1}^M (g_i / \langle g \rangle - 1)^2. \quad (65)$$

This can be written in a form emphasizing local smoothness (rather than global uniformity) a la Tikhonov.

### 5.3.5 Setup

Fix the shape  $\mathcal{B}$ . E.g., a convex polyhedron approximating a sphere can be created by octant triangulation (see lecture notes) or simply by making a latitude-longitude grid and connecting the grid points with lines instead of curves (a “disco ball”). Then the area of a facet is

$$\sigma_j = 2c_j R^2 \sin \Delta\theta \sin \frac{\Delta\varphi}{2} \sin\left(\theta_j - \frac{\Delta\theta}{2}\right), \quad (66)$$

where  $R$  is the sphere radius,

$$c_j = \sqrt{1 - \sin^2 \frac{\Delta\varphi}{2} \cos^2\left(\theta_j - \frac{\Delta\theta}{2}\right)}, \quad (67)$$

and  $\Delta\theta$ ,  $\Delta\varphi$  are the latitude- and longitude intervals and  $\theta_j$  the “southernmost” latitude of the facet ( $\theta$  increases towards “south”). The spherical coordinates  $\nu = (\theta_n, \varphi_n)$  of the direction of the facet’s outward normal are

$$\cos \theta_n = \frac{1}{c_j} \cos \frac{\Delta\varphi}{2} \cos\left(\theta_j - \frac{\Delta\theta}{2}\right), \quad (68)$$

$$\varphi_n = \varphi_j + \frac{\Delta\varphi}{2}, \quad (69)$$

where  $\varphi_j$  is the smaller longitude of the side edges of the facet.

For creating the original maps, give a value  $0 < g_j \leq 1$  for each facet (and plot the maps of your worlds). You can write a black letter over a white surface, make a random map, use a smooth function, etc. Also choose a scattering law, e.g., a linear combination of

$$S_{LS} = \frac{\mu\mu_0}{\mu + \mu_0}, \quad S_L = \mu\mu_0. \quad (70)$$

Generate  $L$  at a number of observing geometries in  $S^2 \times S^2$  using various noise levels. In particular, create series of so-called lightcurve observations at sets of  $\omega = (\vartheta, 0 \leq \psi_i \leq 2\pi), i = 1, \dots, n$  (corresponding to typical time series). Use these data to investigate the inverse problem of reconstructing the world map from  $L$ , especially in the light of the theoretical results discussed in the lecture notes. Remember to avoid inverse crime (typically, use a sparser grid for inversion, or a set of basis functions with which the data are not created).

### 5.3.6 Suggestions and comments

1. Simulate the effects of the number and measurement space coverage of data: what happens with a small set of  $L$ , what if  $\omega_0 \rightarrow \omega$  etc.
2. How small must the noise level be for details of a given size to be discernible in the data (this can be initially checked already via the simulation of the direct problem)?

3. Start with the linear form, check the condition number of your system matrix, see if SVD helps, and so on.
4. Blind test: exchange data sets with your collaborators – is inversion harder now (inverse crime means that you use prior info you are not expected to have in real life).
5. Try the Bayesian approach: use some expected  $g$  distribution for the prior (uniform grayscale, expected letter somewhere, correlation between some facets etc.)
6. Use the nonlinear form and L-M to guarantee  $g > 0$ . Is this more stable? Do you need regularization functions  $R$ ?
7. Use some (smooth) positive function on  $S^2$  to create the values  $g_i$  for constructing simulated data. Are smoothness regularization functions useful? Compare with the letter case. What happens with different discretization levels of the inversion model?
8. How well can different letters as world maps be distinguished? What happens if you use another letter as a priori function?

## 6 Appendix: Levenberg-Marquardt optimization

Let us approximate the nonlinear  $\chi^2$  function

$$\chi^2(a) = \sum_{i=1}^N [f(a; x_i) - L_i]^2, \quad (71)$$

$a \in \mathbb{R}^M$  ( $M$  parameters,  $N$  measurements,  $x \in \mathbb{R}^j$ , some measurement space), by

$$\chi^2(a) \approx C + \nabla \chi^2 \cdot a + \frac{1}{2} a^T D a, \quad (72)$$

with  $\nabla := \partial/\partial a$  and  $D$  the Hessian  $M \times M$  matrix. If the approximation is already a good one (we are near the minimum of  $\chi^2$ ), we hit the optimal  $a_{min}$  by jumping from the current (iterated)  $a_{cur}$  with

$$a_{min} = a_{cur} - D^{-1} \nabla \chi^2(a_{cur}). \quad (73)$$

(This is because a step of length  $-2D^{-1} \nabla \chi^2$  would take us exactly to the other side of the minimum valley, so we take a half of that step to get to the exact centre.) On the other hand, if we are not near the minimum, we could take the steepest descent-type step down the gradient direction:

$$a_{next} = a_{cur} - c \nabla \chi^2(a_{cur}). \quad (74)$$

Now

$$\frac{\partial \chi^2}{\partial a_k} = 2 \sum_i [f(a; x_i) - L_i] \frac{\partial f}{\partial a_k}, \quad (75)$$

and

$$\frac{\partial \chi^2}{\partial a_k \partial a_l} = 2 \sum_i \left[ \frac{\partial f_i}{\partial a_k} \frac{\partial f_i}{\partial a_l} - \mathcal{O}(\epsilon) \right], \quad (76)$$

where we ignore the term of the order of noise level  $\epsilon$  because the uncorrelated  $f(a; x_i) - L_i \sim \pm \epsilon$  contributions tend to cancel each other out. Writing

$$\beta_k := -\frac{1}{2} \frac{\partial \chi^2}{\partial a_k}, \quad \alpha_{kl} := \frac{1}{2} \frac{\partial \chi^2}{\partial a_k \partial a_l}, \quad (77)$$

and the above approximation

$$\alpha_{kl} = \sum_i \frac{\partial f_i}{\partial a_k} \frac{\partial f_i}{\partial a_l}, \quad (78)$$

our “single step to a minimum” can be written as

$$\sum_l \alpha_{kl} \delta a_l = \beta_k, \quad (79)$$

to be solved for the step  $\delta a_l$ . Likewise, the steepest descent reads

$$\delta a_l = c \beta_l. \quad (80)$$

Levenberg-Marquardt combines these two smoothly by using a “fudge” factor  $\lambda$  such that the steepest descent step is given by the choice

$$\delta a_l = \frac{1}{\lambda \alpha_{ll}} \beta_l, \quad (81)$$

and defining

$$\alpha'_{jj} := \alpha_{jj}(1 + \lambda), \quad \alpha'_{jk} = \alpha_{jk}, \quad j \neq k, \quad (82)$$

so the whole thing can be written as

$$\sum_{l=1}^M \alpha'_{kl} \delta a_l = \beta_k. \quad (83)$$

If  $\lambda \gg 1$ , we have the steepest descent domain, while  $\lambda \rightarrow 0$  takes us to the “single step to minimum” regime.

In practice, the Levenberg-Marquardt algorithm is simply:

1. Compute  $\chi^2(a_0)$  for the initial guess  $a_0$ .
2. Choose a small  $\lambda$ , e.g.,  $\lambda = 10^{-3}$ .
3. Solve (83) for  $\delta a$  and evaluate  $\chi^2(a + \delta a)$ .
4. If  $\chi^2(a + \delta a) \geq \chi^2(a)$ , increase  $\lambda \rightarrow 10\lambda$  and go to 3.
5. If  $\chi^2(a + \delta a) < \chi^2(a)$ , decrease  $\lambda \rightarrow \lambda/10$ , update  $a \rightarrow a + \delta a$  and go to 3.

**Stop** if the convergence of  $\chi^2(a)$  has saturated.

L-M is best for a moderate number of unknowns (say, less than 500) as it stores the Hessian matrix (or its approximation). For a large number of unknowns (or functions not writable in  $\chi^2$ -form) it is better to use, e.g., conjugate gradient or other methods that work with an  $M$ -vector instead of an  $M \times M$  matrix.

## References

- [1] B. Carry, C. Dumas, M. Kaasalainen, and 9 colleagues, *Physical properties of 2 Pallas*, *Icarus*, **205** (2010), 460.
- [2] J. Āurech and M. Kaasalainen. *Photometric signatures of highly nonconvex and binary asteroids*, *Astron. Astrophys.*, **404** (2003), 709-714.
- [3] M. Kaasalainen and J. Torppa, *Optimization methods for asteroid lightcurve inversion. I. Shape determination*, *Icarus*, **153** (2001), 24-36.
- [4] M. Kaasalainen, J. Torppa, and K. Muinonen, *Optimization methods for asteroid lightcurve inversion. II. The complete inverse problem*, *Icarus*, **153** (2001), 37-51.
- [5] M. Kaasalainen *Physical models of large number of asteroids from calibrated photometry sparse in time*, *Astron. Astrophys.*, **422** (2004), L39-L42
- [6] M. Kaasalainen and L. Lamberg, *Inverse problems of generalized projection operators*, *Inverse Problems* **22** (2006), 749-769.
- [7] M. Kaasalainen, J. Āurech, B. Warner, Y. Krugly, and N. Gaftonyuk, *Acceleration of the rotation of asteroid 1862 Apollo by radiation torques*, *Nature*, **446** (2007), 420-422.
- [8] M. Kaasalainen, *Multimodal inverse problems: Maximum compatibility estimate and shape reconstruction*, *Inverse Problems and Imaging*, **5** (2011), 37-57.
- [9] L. Lamberg and M. Kaasalainen, *Numerical solution of the Minkowski problem*, *J. Comp. Appl. Math.* **137** (2001), 213-227.
- [10] F. Marchis, M. Kaasalainen, E. Hom, J. Berthier, J. Enriquez, D. Hestroffer, D. Le Mignant, and I. de Pater, *Shape, size and multiplicity of main-belt asteroids. I. Keck adaptive optics survey*, *Icarus*, **185** (2006), 39-63.
- [11] H. Minkowski *Volumen und Oberflache*, *Math. Ann.*, **57** (1903), 447-495
- [12] L. Nirenberg *The Weyl and Minkowski problems in differential geometry in the large*, *Comm. Pure Appl. Math.*, **6** (1953), 337-394